

Revealing the magnetic field in a distant galaxy cluster: discovery of the complex radio emission from MACS J0717.5 +3745

A. Bonafede^{1,2}, L. Feretti², G. Giovannini^{1,2}, F. Govoni³, M. Murgia^{2,3}, G. B. Taylor⁴, H. Ebeling⁵, S. Allen⁶, G. Gentile^{7,8}, and Y. Pihlström⁴

¹ Università di Bologna, Dip. di Astronomia, via Ranzani 1, 40126 Bologna, Italy
e-mail: bonafede@ira.inaf.it

² INAF, Istituto di Radioastronomia, via Gobetti 101, 40129 Bologna, Italy

³ INAF, Osservatorio Astronomico di Cagliari, Strada 54, Loc. Poggio dei Pini, 09012 Capoterra (Ca), Italy

⁴ Department of Physics and Astronomy, University of New Mexico, Albuquerque, NM 87131 and Adjunct Astronomer at the National Radio Astronomy Observatory, USA

⁵ Institute for Astronomy, University of Hawaii, 2680 Woodlawn Drive, Honolulu, HI 96822, USA

⁶ Kavli Institute for Particle Astrophysics and Cosmology, Stanford University, 382 Via Pueblo Mall, Stanford, CA 94305-4060, USA

⁷ Institut d'Astronomie et d'Astrophysique, Faculté des Sciences, Université Libre de Bruxelles, CP 226, Bvd du Triomphe, 1050 Bruxelles, Belgium

⁸ Sterrenkundig Observatorium, Universiteit Gent, Krijgslaan 281, 9000 Gent, Belgium

Received 18 May 2009 / Accepted 2 July 2009

ABSTRACT

Aims. To study at multiple frequencies the radio emission arising from the massive galaxy cluster MACS J0717.5+3745 ($z = 0.55$). Known to be an extremely complex cluster merger, the system is uniquely suited for an investigation of the phenomena at work in the intra-cluster medium (ICM) during cluster collisions.

Methods. We use multi-frequency and multi-resolution data obtained with the Very Large Array radio telescope, and X-ray features revealed by Chandra, to probe the non-thermal and thermal components of the ICM, their relations and interactions.

Results. The cluster shows highly complex radio emission. A bright, giant radio halo is detected at frequencies as high as 4.8 GHz. MACS J0717.5+3745 is the most distant cluster currently known to host a radio halo. This radio halo is also the most powerful ever observed, and the second case for which polarized radio emission has been detected, indicating that the magnetic field is ordered on large scales.

Key words. galaxies: clusters: general – galaxies: clusters: individual: MACS J0717+3745 – radiation mechanisms: non-thermal – polarization – magnetic fields

1. Introduction

A detailed description of the physical conditions and energetics of the intra-cluster medium (ICM) in galaxy clusters requires adequate knowledge of the role of the non-thermal components: relativistic particles and magnetic fields. In recent years, non-thermal ICM emission and its connection with highly energetic events occurring during cluster mergers has become a much researched and discussed topic. Radio halos and radio relics are suspected to be the signature of mergers, although their origin and evolution is still the subject of considerable debate. Radio halos have now been observed in the central region of several clusters of galaxies. With the exception of the radio halo in Abell 2255 (Govoni et al. 2005), they are not polarized, and their spectrum¹ is steep ($\alpha > 1$). Radio halo emission is likely due to the re-acceleration of electrons permeating the cluster volume (see e.g. Brunetti et al. 2008). By contrast, radio relics are usually observed at the periphery of galaxy clusters. They vary widely in morphology and size and are polarized at a level of 20–30% at 1.4 GHz. They also exhibit steep radio spectra and are thought to be generated by shocks occurring in the ICM during merger

events (see e.g. Roettiger et al. 1999; Hoeft & Brueggen 2007). Both radio-halo and radio-relic emission indicate the presence of a $\sim\mu\text{G}$ magnetic field in the ICM.

In recent years, the presence of magnetic fields in galaxy clusters has been unambiguously established, and their importance for our understanding of the physical processes at work in the ICM has been recognized (see e.g. the reviews by Carilli & Taylor 2002; Govoni & Feretti 2004; Ferrari et al. 2008; Dolag et al. 2008). Magnetic fields are able to inhibit transport processes like heat conduction, spatial mixing of gas, and the propagation of cosmic rays. Values of the Faraday Rotation Measure (RM) have been determined both for radio galaxies within and behind the cluster, using statistical samples (e.g. Kim et al. 1991; Clarke 2004; Johnston-Hollitt et al. 2004) as well as individual clusters by analyzing high-resolution images (e.g. Taylor & Perley 1993; Feretti et al. 1995; Govoni et al. 2006). The results are consistent with the presence of magnetic fields of $\sim\mu\text{G}$ throughout the cluster, in agreement with predictions from cosmological MHD simulations (Dolag & Staszczyn 2008; Donnert et al. 2009). These studies also indicate that the magnetic fields in the ICM are structured on scales as low as 10 kpc, and possibly even less. Work on magnetic fields in clusters has, so far, focused on relatively nearby systems ($z < 0.4$), with much

¹ We define the radio spectrum as $S(\nu) \propto \nu^{-\alpha}$, where α is the spectral index and S the observed flux density at frequency ν

less information being available for clusters at higher redshift. Extending the redshift range of such studies is crucial because of their importance to the subject of the formation and evolution cosmic magnetic fields, and to investigate how the strength and structure of magnetic fields in clusters is connected to the systems' dynamic history.

MACS J0717.5+3745 (MACS J0717; $z = 0.55$) was discovered in the Massive Cluster Survey (MACS; Ebeling et al. 2001) and has since been found to be one of the most disturbed galaxy clusters known at any redshift. It is part of the statistically complete sample of the twelve most distant MACS clusters, all of which lie at $z > 0.5$ (Ebeling et al. 2007). In-depth optical and X-ray studies of the galaxy population and the ICM of MACS J0717 identified it as one of the most promising targets for studies of the physical mechanisms governing merger events (Ebeling et al. 2004; Ma et al. 2008, 2009).

Our detailed study of the radio emission arising from both galaxies and the ICM of this cluster is prompted by the work of Edge et al. (2003) who discovered a radio relic in MACS J0717 when analyzing data from the Faint Images of the Radio Sky at Twenty-cm (FIRST, Becker et al. 1995) survey. Since radio emission is indicative of the presence of a magnetic field, such observations are the most direct way to obtain information of this fundamental ingredient in the physics of the ICM.

In Sects. 2 and 3 we summarize our present knowledge of this cluster based on previous optical and X-ray studies. Radio observations and data reduction techniques are described in Sect. 4. In Sects. 5 and 6 we discuss the total-intensity emission from the radio galaxies and from the ICM. In Sect. 7 we analyze the polarization properties of the radio emission, while in Sect. 8 results for the Faraday Rotation are presented and discussed. The spectral index and the magnetic field properties of this cluster are the subjects of Sects. 9 and 10. Finally, conclusions are presented in Sect. 11. We use the concordance cosmological model Λ CDM, with $H_0 = 71 \text{ km s}^{-1} \text{ Mpc}^{-1}$, $\Omega_M = 0.27$, and $\Omega_\Lambda = 0.73$. In this cosmology, at redshift $z = 0.55$, 1 arcsecond corresponds to a scale of 6.394 kpc.

2. Optical observations

The complex optical morphology of MACS J0717 was first noted by Edge et al. (2003), based on imaging in the *V*, *R*, and *I* passbands obtained with the University of Hawaii 2.2 m telescope. Much deeper observations conducted since with SuprimeCam, the wide-field imager at the prime focus of the Subaru 8 m telescope, firmly established MACS J0717 as a highly disturbed merger and led to the discovery of a 6-Mpc long filament leading into the cluster from the south-east (Ebeling et al. 2004). Spectroscopic observations of over a thousand galaxies in the field of MACS J0717 have been performed in order to probe its spatial and kinematic structure along the line of sight, and to characterize the galaxy population as a function of cluster environment (Ma et al. 2008). Finally, space-based observations with the Advanced Camera for Surveys (ACS) aboard the Hubble Space Telescope (GO-09722, PI Ebeling) provided a high-resolution view of MACS J0717, including the interface region where the filament meets the dynamically most active central region of the cluster.

3. X-ray observations

With an X-ray luminosity of $(2.74 \pm 0.03) \times 10^{45} \text{ erg/s}$ in the 0.1–2.4 keV energy band (Ebeling et al. 2007) MACS J0717

is one of the most X-ray luminous clusters known at $z > 0.5$. The cluster was observed with the ACIS-I instrument aboard the Chandra X-ray Observatory for a total exposure time of 60 ks (ObsID 4200). A detailed study of the system's X-ray properties was recently performed by Ma et al. (2008, 2009). Their spatial description of the gas distribution uses a β -model (Cavaliere & Fusco-Femiano 1976):

$$\rho_{\text{gas}} = \rho_0 \left[1 + \frac{r^2}{r_c^2} \right]^{-\frac{3\beta}{2}} \quad (1)$$

where ρ_{gas} is the gas density, r is the radial distance from the cluster center, and r_c is the cluster core radius. By fitting this model to the X-ray surface brightness data, they derived $\beta = 1.1 \pm 0.1$, $r_c = 92'' \pm 6''$ and $\rho_0 = 1.71 \pm 0.05 \times 10^{14} M_\odot \text{ Mpc}^{-3}$. Ma and co-workers report the detection of X-ray emission from the filament and, for the main cluster, a very complex X-ray morphology, including dramatic variations in the intra-cluster gas temperature, with extreme values of 5 and over 20 keV (the average gas temperature quoted by Ebeling et al. 2007 is 11 keV). The authors' joint optical/X-ray analysis of all available data identifies the filament as the source of both continuous and discrete accretion of matter by the cluster from a south-easterly direction, and isolates four distinct subclusters participating in an ongoing triple merger. The X-ray emission from MACS J0717 and the cluster-filament interface is shown in Fig. 1.

4. Radio observations and data reduction

We investigate the radio emission from MACS J0717 with multi-frequency and multi-resolution VLA observations. Specifically, we performed new high-resolution observations in full-polarization mode. These observations focused on radio galaxies in the field, as well as on the relic, to study their Faraday rotation measure. In addition, new low-resolution observations were performed to study the diffuse emission of the cluster. We also used archival VLA observations, both of high and low resolution, as specified below.

4.1. High-resolution observations

MACS J0717 was observed with the B array at four frequencies within the 20-cm band (1.365 GHz, 1.435 GHz, 1.485 GHz, and 1.665 GHz), and with the C array at two frequencies within the 6-cm band (4.535 GHz, and 4.885 GHz). The targets of these observations were the relic, the radio galaxy embedded in the relic emission (labelled A in Fig. 1) and the radio galaxies labelled B and C in Fig. 1 detected at larger projected distance from the cluster center. Two separate pointings were necessary at 6 cm to avoid bandwidth and primary-beam attenuation. The source 0137+331 (3C48) was used as the primary flux-density calibrator, and the source 0521+166 (3C138) as an absolute reference for the electric vector polarization angle. The nearby source 0713+438 was observed at intervals of ~ 20 min and used as phase calibrator. Calibration and imaging were performed with the NRAO Astronomical Image Processing System (AIPS), following standard procedures. Self-calibration was performed to refine antenna phase solutions, followed by a final gain and amplitude self-calibration cycle. Images of the total intensity (Stokes *I*), as well as of the Stokes parameters *U* and *Q*, were produced for each frequency separately. We then derived images of the polarized intensity $P = \sqrt{(Q^2 + U^2)}$ and of the polarization angle $\Psi = 0.5 \arctan(U/Q)$. These images were

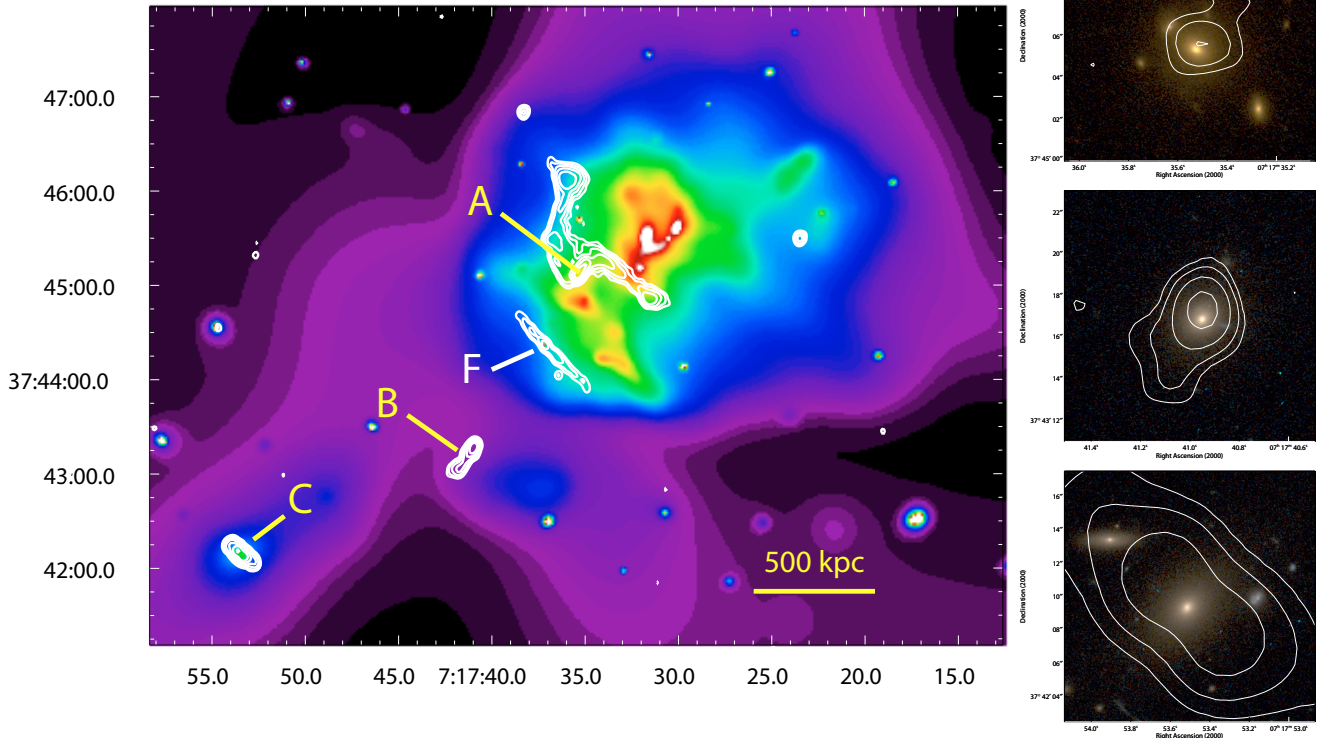


Fig. 1. Image of the X-ray surface brightness of MACS J0717 as observed with Chandra in the 0.5–7 keV band, adaptively smoothed using the *asmooth* algorithm (Ebeling et al. 2006) requiring a minimal significance of 99% with respect to the local background. Contours show the emission from radio sources at 1.365 GHz. The size of the restoring beam is $5'' \times 4''$, and the rms noise is $\sigma \sim 3.0 \mu\text{Jy}/\text{beam}$. The lowest contour level corresponds to 5σ , additional contours are spaced by factors of 2. The source labelled F is a foreground radio galaxy. The side panels show contours of the radio emission from sources A, B, and C (top to bottom), overlaid on optical images obtained with the Hubble Space Telescope (HST). For sources A and B, we show the emission at 8.460 GHz, where the restoring beam is $2.4'' \times 2''$, and the rms noise $\sigma \sim 0.04 \text{ mJy}/\text{beam}$. The first contour is placed at the 3σ level; additional contours are spaced by factors of 2. Radio emission from source C is shown at 1.365 GHz, using the same contour levels as in the large image. The HST images were obtained with the Advanced Camera for Surveys (ACS), using the F555W and F814W filters (source A), and the F606W and F814W passbands (source B and C).

Table 1. Radio observations.

Project Id	RA (J2000)	Dec (J2000)	ν (GHz)	Bandwidth (MHz)	Configuration	Date	ToS (Hours)	Restoring beam $'' \times ''$	rms noise (mJy/beam)
AG761	07h17m35.0s	37d45'07"	1.365–1.435	25	B	16-Dec.-07	2.2	5×4	0.030
AG761	07h17m35.0s	37d45'07"	1.485–1.665	25	B	24-Dec.-07	2.8	5×4	0.025
AG761	07h17m35.0s	37d45'07"	4.885–4.535	50	C	24-Mar.-08	2.4	5×4	0.015
AG761	07h17m53.0s	37d42'11"	4.885–4.535	50	C	20-Apr.-08	2.2	5×4	0.016
AT0358	07h17m30.9s	37d45'30"	1.425	50	C	15-Mar.-08	1.8	18×14	0.020
AH748	07h17m33.8s	37d45'20"	4.860	50	D	27-Nov.-01	1.5	18×14	0.020
AE0125	07h17m35.4s	37d45'07"	8.460	50	C	22-Nov.-1998	0.2	2.4×2	0.04

restored with a Gaussian beam of $FWHM = 5'' \times 4''$ which corresponds to a linear resolution of $\sim 32 \text{ kpc}$. In order to distinguish the relic emission from that of embedded radio sources we have retrieved from the NRAO archive a short ($\sim 10 \text{ min}$) observation performed at 8.460 GHz (project ID AE125). Here the source 3C 147 was used as primary flux-density calibrator, and the source 0741+312 was used as phase calibrator. Because of the smaller field of view, only the sources A and B are visible in the radio image. Observational details are reported in Table 1.

4.2. Low-resolution observations

MACS J0717 was observed with the C array at 1.425 GHz in order to properly image the extended emission. The source

1331+305 (3C 286) was used as primary flux-density calibrator, and also as an absolute reference for the electric vector polarization angle. The source 0713+438 was used as phase calibrator. Calibration and imaging were performed with the NRAO Astronomical Image Processing System (AIPS), following standard procedures. In addition, we recovered from the VLA data archive an observation at 4.860 GHz (project ID AH748). Here the source 0714+335 was used as phase calibrator. At both frequencies total-intensity maps (Stokes I) were produced using natural weighting and restored with the same beam of $FWHM \sim 18'' \times 14''$, corresponding to $\sim 100 \text{ kpc}$. In order to study the diffuse polarized emission, I , Q , and U images were also produced from 1.425 GHz observations at low resolution ($FWHM \sim 21 \sim 18''$). Observational details are reported in Table 1.

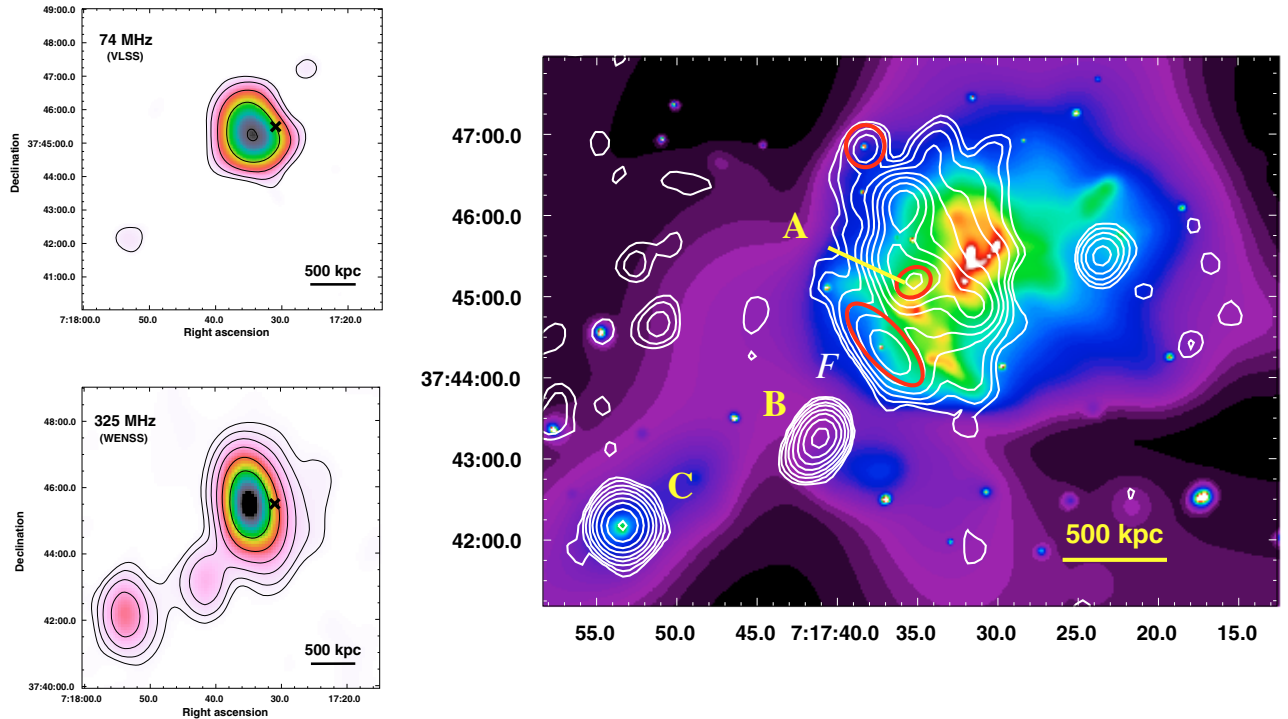


Fig. 2. Radio emission from MACS J0717 at 74 MHz from the VLSS (*top left*), and at 325 MHz from the WENSS (*bottom left*). Contour levels start at 3σ (i.e. 0.24 Jy/beam for the VLSS image and 9 mJy/beam for the WENSS image) and are then spaced by factors of 2. The cross marks the X-ray center. See text for details. *Right*: Contours of the radio emission at 1.425 GHz and at low resolution, overlaid on a image of the X-ray emission as observed with Chandra (see caption of Fig. 1). Contour levels start at 9 mJy/beam (3σ); subsequent contour levels are spaced by factors of 2. The *FWHM* of the restoring beam is $\sim 21'' \times 18''$. Circles and ellipse mark sources embedded in the radio-halo emission.

Table 2. Total and polarization-intensity radio emission.

Name	RA (J2000)	Dec (J2000)	dist kpc	ν GHz	Peak brightness (mJy/beam)	Flux density (mJy)	Peak of pol. flux (mJy/beam)
Source A	07h17m35.4s	+37d45'08''	450	1.365	8.3	22.2	0.3
				1.435	8.4	22.4	0.3
				1.485	7.7	20.0	0.2
				1.665	7.4	18.1	0.3
				4.535	2.3	4.7	0.2
				4.885	2.1	3.9	0.2
				8.460	0.5	0.7	
				8.460	1.6	1.9	
Source B	07h17m40.9s	+37d43'17''	1150	1.365	9.2	19.9	0.2
				1.435	9.3	18.8	0.3
				1.485	8.8	18.3	0.4
				1.665	8.8	18.3	0.4
				4.535	4.1	7.0	0.3
				4.885	3.8	6.4	0.2
				8.460	1.6	1.9	
				8.460	1.6	1.9	
Source C	07h17m53.7s	+37d42'11''	2140	1.365	10.0	32.8	0.1
				1.435	9.9	32.3	0.2
				1.485	9.6	30.5	0.2
				1.665	9.8	30.4	0.2
				4.535	5.4	17.2	0.5
				4.885	5.0	14.7	0.4

5. Radio emission: the relic-filament structure and the radio galaxies

The presence of non-thermal emission associated with the ICM in MACS J0717 was first reported by Edge et al. (2003) who classified the emission as a relic. The wealth of radio data described in the previous section allows a multi-resolution and

multi-frequency study of the radio emission arising from this cluster. Figure 1 shows the 1.365 GHz data from VLA B-array observations in contours, overlaid on the X-ray surface brightness in colors. The radio data reveal a bright, filamentary structure whose central part is coincident with the relic discovered by Edge et al. (2003). In addition, several radio sources are detected. Those related to the cluster and the large-scale optical

and X-ray filament are labelled A, B, and C, whereas the source labelled F is a radio galaxy in the foreground ($z = 0.1546$, Ma et al., in preparation).

A proper study of the extended emission associated with the ICM needs to take into account possible contamination from radio galaxies embedded in the diffuse emission. This can be done with the help of high-resolution and high-frequency observations in which the extended emission is resolved out and too faint to be detected. Using 8.460 GHz observations we have identified one such embedded radio galaxy, labelled A in Fig. 1 and shown in a close-up view in the side panel of the same figure. This source is $\sim 70''$ away from the cluster center in projection. It consists of a bright region, likely the core of the radio galaxy, with a spectral index of ~ 0.7 between 1.465 GHz and 4.885 GHz, and an extended, more diffuse region extending toward the NW. The spectral index steepens up to ~ 2 with increasing distance from the core. The optical counterpart coincides with the radio core (Fig. 1).

Moving out from the cluster center, two additional radio galaxies, labeled B and C in Fig. 1, are visible at all the observed frequencies. Both are located to the SE of the cluster's X-ray center, at projected distances of $\sim 180''$ and $\sim 335''$, respectively. We note their position along the X-ray and optical large-scale filament detected by Ebeling et al. (2004). Source C is the brightest cluster galaxy of the next cluster (also detected in the Chandra observation) that is going to merge with MACS J0717. In Table 2 we report the main radio properties of the identified radio galaxies at the observed frequencies. The optical counterparts of A, B, and C are all spectroscopically confirmed to lie at redshifts consistent with that of MACS J0717 proper.

6. The radio halo

Being sensitive to structure on larger angular scales, observations performed with the C array at 1.425 GHz and with D array at 4.860 GHz reveal the presence of an extended radio halo permeating the cluster volume around the filamentary structure visible at high resolution and discussed in the previous section. MACS J0717 is the most distant cluster in which a radio halo has been observed so far and its presence, together with the radio halo detected in the cluster CL0016 by Giovannini & Feretti (2000) at $z = 0.54$, indicates that the ICM is already significantly magnetized at redshift $z \sim 0.5$. The detection of yet more extended emission around the filamentary structure detected at higher resolution raises some questions about the nature and origin of the latter. This structure could either be a radio relic located at the cluster periphery, but appearing close to the cluster center when viewed in projection, or it could be a filamentary feature that is in fact part of the radio halo. We will further investigate these hypotheses with the help of additional information on the polarization and spectral index of the radio emission (see Sects. 8 and 9). In the following analysis, we will refer to this feature as the relic-filament in order to stress its uncertain nature.

In Fig. 2 the halo emission at 1.425 GHz is shown overlaid onto the cluster X-ray emission. The maximal angular extent of the halo at 1.425 GHz is $\sim 240''$ in the NS direction, corresponding to a linear size of ~ 1.5 Mpc. At 4.860 GHz only the brightest regions of the halo are visible, and its angular extent is reduced to $\sim 160''$ (i. e. ~ 1 Mpc).

As shown in the panels on the left of Fig. 2, the radio halo in MACS J0717 is also detected at 74 MHz in the VLSS (VLA Low Sky Survey, Cohen et al. 2007), and at 325 MHz in the Westerbork Northern Sky Survey (WENSS,

Rengelink et al. 1997). The VLSS was performed with the B array at a resolution of $80'' \times 80''$ and with an rms noise level of ~ 0.08 Jy/beam, while the WENSS has a resolution of $54'' \times 54'' \cos(\text{DEC})$, which translates into $54'' \times 84''$ for the declination of MACS J0717. The apparent angular extent of the halo in the WENSS image is $\sim 280''$, corresponding to ~ 1.8 Mpc. Furthermore, faint radio emission that appears to connect the radio galaxies B and C with the central halo is detected at 325 MHz at 3σ significance. We note that this region coincides with the large-scale filament funneling matter onto MACS J0717 that has been detected at optical and X-ray wavelengths by Ebeling et al. (2004) and Ma et al. (2009). The detection of radio emission in this area might indicate that the magnetic field is already present in the filament before the amplification due to the merger process has occurred. However, the feature is detected at 3σ significance and could simply be the result of blending of the two radiosources B and C at the low resolution of the 325 MHz data. Deeper observations would be required to clarify this issue.

7. Polarized emission from the ICM

High-resolution observations were performed in full-polarization mode, as well as 1.425 GHz observations at low resolution. We are thus able to study the polarized emission in a wide range of resolutions, and, at high resolution, in a wide range of frequencies.

7.1. High-resolution images

The relic-filament is located $\sim 40''$ (~ 260 kpc in projection) SE of the main X-ray peak of the cluster. Its maximal angular extent is $\sim 130''$ at 1.4 GHz, corresponding to ~ 830 kpc at the cluster redshift, and its orientation is $\sim 30^\circ$. Its flux density (excluding the region covered by source A) is ~ 83 mJy at 1.365 GHz, and ~ 16 mJy at 4.885 GHz.

The relic-filament is polarized at all of the observed frequencies. Its mean fractional polarization is 8% at 1.365 GHz and increases to 17% at 4.885 GHz. These values are consistent with those found in other relics, as well as with the values found in the filament of the radio halo in Abell 2255 (Govoni et al. 2005). In Fig. 3 the E-vectors at 1.365 and 4.885 GHz are shown. We note that the polarization of the relic-filament is not uniform. Its northern part is strongly depolarized at 1.365 GHz. Its mean fractional polarization is a few percent at 1.365 GHz and increases to 20% at 4.885 GHz. Depolarization between 1.365 and 4.885 GHz also occurs in the southern part, as expected, but is less dramatic (the mean fractional polarization is $\sim 9\%$ at 1.365 GHz and $\sim 16\%$ at 4.885 GHz).

7.2. Low-resolution images

In order to reveal any extended emission from the radio halo, an image was produced using a Gaussian taper to down weight long-baseline data points in the UV plane. The image was then restored with a Gaussian beam of $FWHM \sim 21'' \times 18''$ (see Fig. 2).

In order to investigate the presence of polarized emission from the radio halo we produced Stokes Q and U radio images following the same technique. We then derived the polarization angle image and the polarization intensity image without imposing any cut. From the polarization intensity image we derived the fractional polarization image by dividing the polarization intensity image to the total intensity image, and we considered as

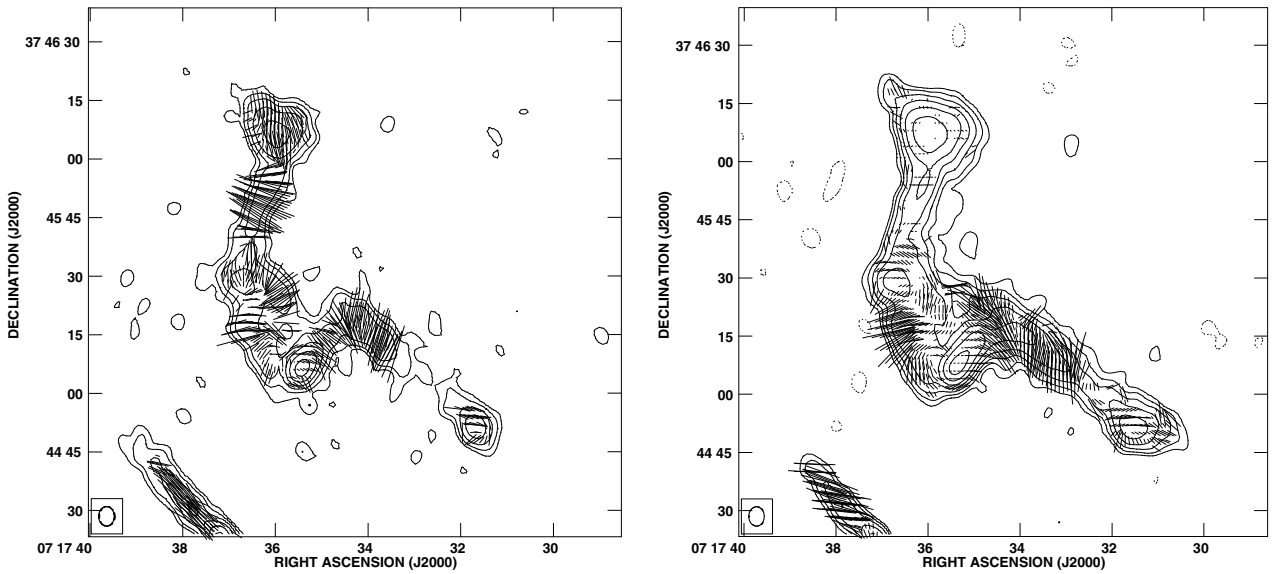


Fig. 3. Polarized emission from MACS J0717 at 4.885 GHz (*left panel*) and at 1.365 GHz (*right panel*). Contours represent the total intensity. The *FWHM* of the restoring beam is $5'' \times 4''$. The lowest contours shown are at -3σ and 3σ ; subsequent contours are spaced by factors of 2. Lines represent the polarization vectors: line orientation indicates the direction of the E field, while line length is proportional to the polarization percentage. $1''$ corresponds to 3%.

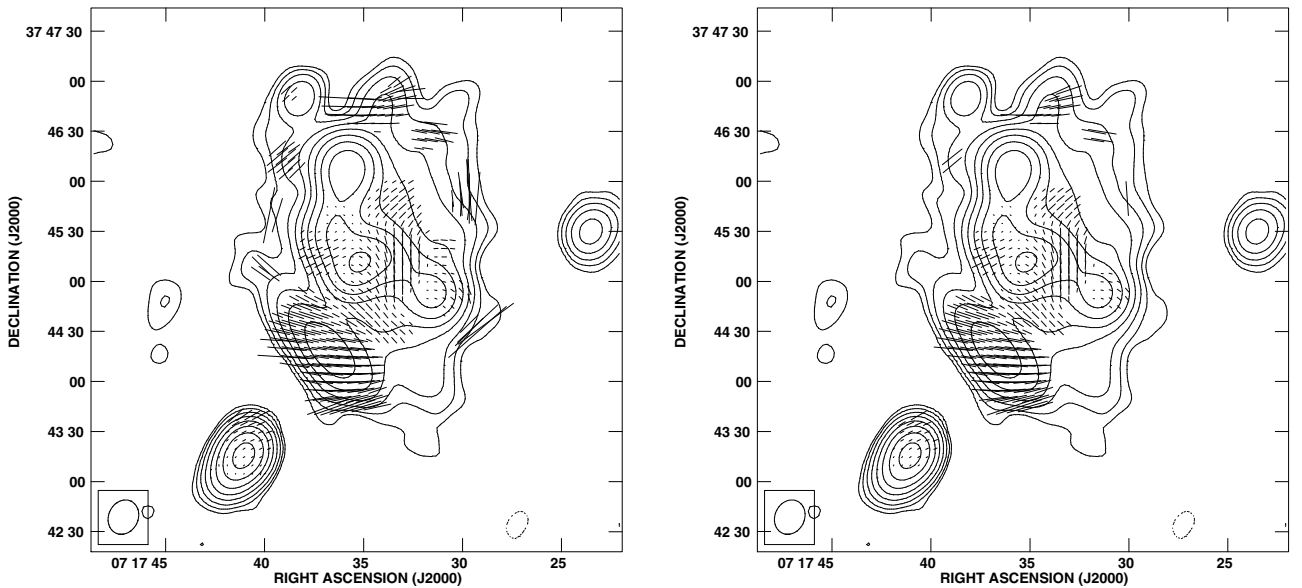


Fig. 4. Polarized emission from the cluster at 1.425 GHz. Contours show to the total-intensity emission at the resolution of $21'' \times 18''$, starting at 3σ , with higher contour levels spaced by factors of 2. Lines refer to the E vectors. Their orientation represents the projected E-field not corrected for Galactic rotation. Their length is proportional to the fractional polarization: $1''$ corresponds to 1.3%. Fractional polarization pixels with a signal-to-noise ratio less than 3 (*left*) and 5 (*right*) were blanked (see text).

valid pixels those whose signal-to-noise ratio was >3 , and >5 in the output image. The cut on the final image, done on the basis of the signal-to-noise ratio, is done to get rid of possible spurious polarization. The resulting images are shown in Fig. 4. From them we can gather that there is a detection of polarization in the halo, mostly concentrated in one region in the center, and also strong at the edges, though this becomes weaker when the cut on the fractional polarization images are more severe.

From Fig. 4 we can also gather some indication that the radio emission detected at high resolution and previously classified as relic is likely a polarized filament belonging to the radio halo. We note, in fact that the polarized structure as revealed from the polarization vectors does not show any jump between the relic and the more extended part, but instead the E-vectors trace with continuity the brightest part of the radio halo. We refer, for comparison to the case of Abell 2256 (Clarke & Ensslin 2006). Here

the polarized emission image marks a clear and sharp distinction between the radio halo and the radio relic. Thus, we report the polarization percentage values of the whole ICM emission (excluding only the contribution of source A). The mean polarization percentage at 1.425 GHz is $\sim 2\text{--}7\%$, ($3\text{--}5\sigma$ detection) with lower value in the central part of the halo, that is $\sim 0.01\text{--}0.6\%$ ($3\text{--}5\sigma$ detection) and higher values at the edges, where it reaches a maximum value of $\sim 24\text{--}34\%$ ($3\text{--}5\sigma$ detection). We note that values reported here based on low-resolution observations might be affected by beam depolarization. Indeed, small-scale variations of the magnetic-field orientation are evident from high-resolution images (see Fig. 3). At 20 cm we get 1 radian of rotation for a RM of 25 rad/m^2 (see Eq. (2)), thus for a $20''$ beam the RM gradient is about $1 \text{ rad/m}^2/''$ to cause cancellation within the beam, and any reasonable ICM model could produce this. Therefore the mean polarization percentages should be considered lower limits.

8. Rotation Measures

Since synchrotron radiation is linearly polarized, its interaction with the magnetized ICM results in a rotation of the wave polarization plane, called Faraday Rotation. If the radiation passes through an external screen, the observed polarization angle Ψ_{obs} at a wavelength λ is related to the intrinsic one Ψ_{int} by the relation

$$\Psi_{\text{obs}} = \Psi_{\text{int}} + \lambda^2 \times RM. \quad (2)$$

Here RM is the Rotation Measure, which is related to the gas density n and to the magnetic field intensity along the line of sight according to:

$$RM \propto \int_{\text{los}} nB_{\parallel} dl. \quad (3)$$

The situation in this cluster could however be much more complicated than the drawn picture. If radiation is strongly affected by beam depolarization, or if the Faraday rotation is internal, Eq. (2) is not applicable (see Burn 1966). The large frequency range of our observations allows us to test whether a simple linear fit of the polarization angle versus λ^2 is consistent with our data.

8.1. Rotation Measure fits

We performed a fit of the polarization angle images as a function of λ^2 for the relic-filament, and for the sources B and C. We used the PACERMAN algorithm (Polarization Angle Correcting Rotation Measure ANalysis) developed by Dolag et al. (2005). The algorithm solves the $n\pi$ ambiguity in low signal-to-noise regions exploiting the information of nearby reference pixels, under the assumption that the reference pixel is connected to the nearby areas as far as the polarization angle gradient is under a certain threshold in all of the observed frequency maps simultaneously. We considered as reference pixel those which have a polarization angle uncertainty smaller than 7 degrees, and fixed the gradient threshold to 15 degrees. 7 degree error of the polarization angle corresponds to 3σ level in both U and Q polarization maps simultaneously.

We note that some regions show a high polarized flux at 6 cm while they are weakly polarized at 20 cm. This could indicate that the Faraday rotation is higher in these regions, leading to higher depolarization in lower frequency observations. Excluding these regions would correspond to a bias toward low

RM regions. So we decided to allow PACERMAN to perform the RM fit if at least in 3 frequency maps the above mentioned conditions were satisfied.

Once the RM image is obtained, the galactic contribution to the observed RM must be subtracted. We computed the average RM for extragalactic sources from the catalog published by Simard-Normandin et al. (1981). The cluster's galactic coordinates are: lon = 180.25° and lat = $+21.05^\circ$. It results that in a region of $15^\circ \times 15^\circ$ centered on the cluster the Galactic contribution is $\sim 17 \text{ rad/m}^2$. This value is also consistent with the $\langle RM \rangle$ that we find in our observations for the foreground galaxy F located at $07^{\text{h}}17^{\text{m}}37.2^{\text{s}}, +37^\circ44'21''$ (J2000). Its $\langle RM \rangle$ is $15 \pm 3 \text{ rad/m}^2$, with values going from -3 rad/m^2 to 28 rad/m^2 .

8.1.1. RM fit in the relic-filament region

From the existing data we can only derive the position of the relic-filament in projection, but not where it lies with respect to MACS J0717 along the line of sight. It could be a foreground structure (case 1), a background structure (case 2) seen in projection, or a bright part of the radio halo neither behind or in front of the cluster (case 3). The polarization properties and the trend of the polarization angle versus λ^2 can help in distinguish among these three situations, and we will discuss them in the following.

- **Case 1:** our galaxy acts like a Faraday screen, similarly to what we observe for the foreground source F, so we expect to obtain $RM \sim 10 \text{ s rad/m}^2$.
- **Case 2:** the ICM acts like a Faraday screen and the polarization angle rotates following Eq. (2).
- **Case 3:** in this case the situation is much more complicated. The trend of Ψ versus λ^2 may result from complex geometries (see Burns 1966). In this case the rotation does not originate in an external Faraday screen, Eq. (2) does not hold anymore, and obtaining information about the magnetic field from Faraday rotation requires detailed knowledge of the ICM distribution and properties.

In Fig. 5 we show fits of Ψ versus λ^2 obtained in the relic-filament region. The poor agreement between the data and the simple linear model suggests that the Faraday rotation is not occurring in a Faraday screen, thus favouring scenario (3) above. The observed trends of Ψ versus λ^2 are also incompatible with internal Faraday rotation generated by a uniform slab (see Burn 1966). Although strong beam depolarization could affect the trend of Ψ versus λ^2 , present data favour the third scenario and suggest that the relic-filament is actually a polarized filament belonging to the radio halo and not a radio relic connected to a peripheral merging shock.

8.1.2. RM fit for the sources B and C

In Fig. 6 we show the RM image and plots of Ψ versus λ^2 obtained with PACERMAN for the two radio sources B and C. The fits shown confirm that, as expected, the RM observed here is due to an external Faraday screen. In Table 3 we report the observed RM for these sources (RM_{obs}) and the RM in the cluster rest frame (RM_{crf}), that is given by $RM_{\text{crf}} = RM_{\text{obs}} \times (1 + z)^2$. Once the Galactic contribution is subtracted, we obtain $\langle RM_{\text{crf}} \rangle$ values of $-312 \pm 1 \text{ rad/m}^2$ and $204 \pm 1 \text{ rad/m}^2$ for sources B and C, respectively. As source C is associated with the BCG of a satellite cluster embedded in the large-scale filament and visible in the X-ray image, its RM is representative of the properties of

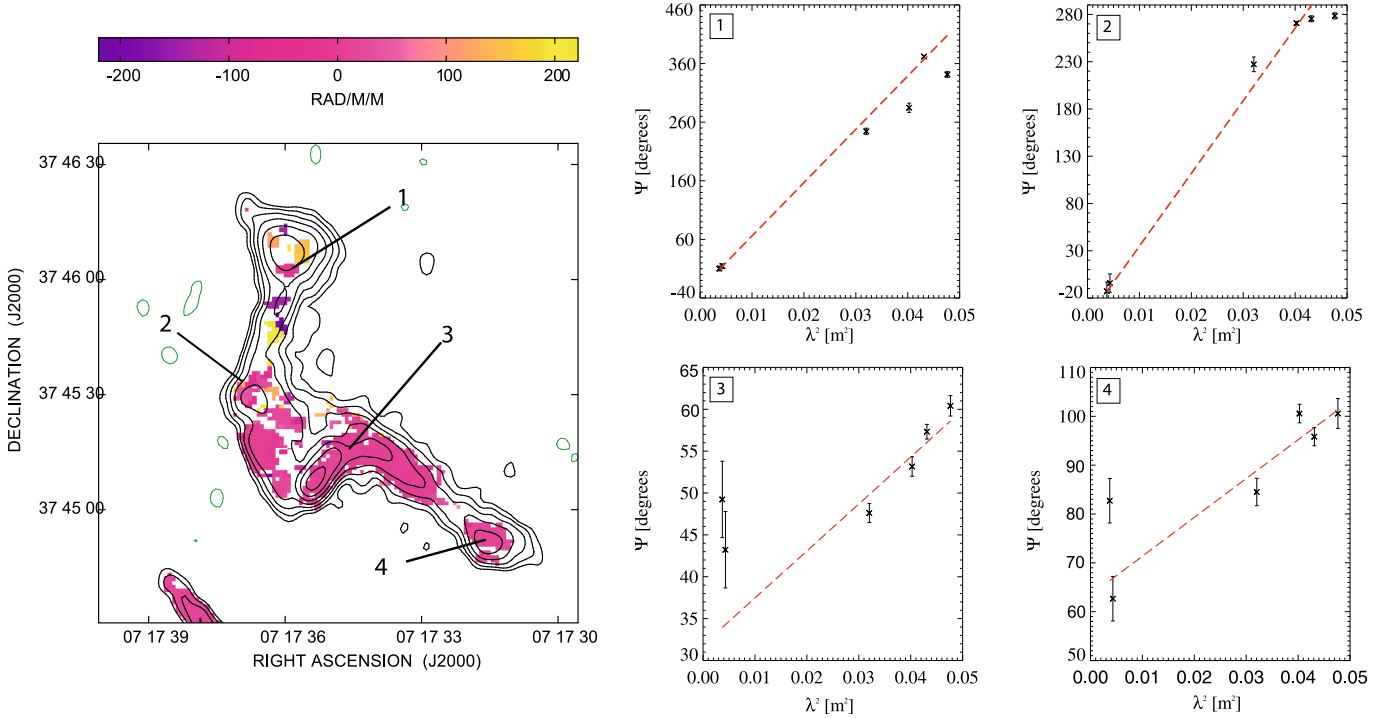


Fig. 5. *Left panel:* Contours refer to the radio emission at 1.425 GHz. The restoring beam $FWHM$ is $5'' \times 4''$. The image represents the attempt to fit the Polarization Angle at the observed frequencies with the λ^2 law in the relic-filament region. Results from fits of a λ^2 law to the polarization angle are shown in the plots on the *right*. They refer to four random pixels located in different parts of the relic-filament and of the source A as indicated in the *left panel*.

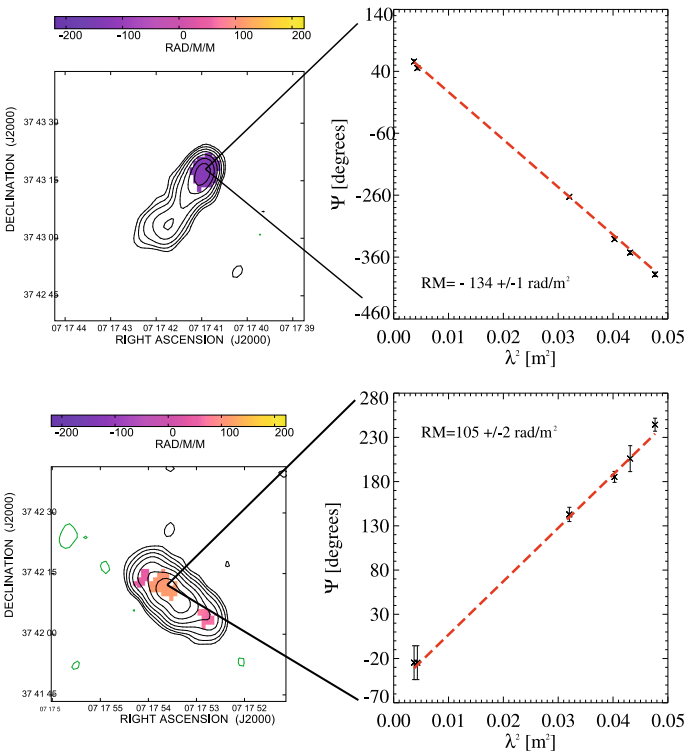


Fig. 6. *Left:* Observed rotation measure images obtained for the source B (*top panel*) and C (*bottom panel*). *Right panel:* fit of the Polarization angles Ψ versus λ^2 , demonstrating that the Faraday rotation is occurring in a foreground screen. The fits are referred to a representative pixel in the two sources.

that cluster. There is no obvious concentration of X-ray emission around source B, which is also located along the optical

Table 3. RM values for sources B and C.

Name	$\langle RM_{\text{obs}} \rangle$ rad/m ²	$\langle RM_{\text{crr}} \rangle$ rad/m ²	Fit error (average) rad/m ²	N of beams
Source B	-130	-312	1	3
Source C	85	204	1	3

Column 1: Source name ; Col 2: observed $\langle RM \rangle$; Col 3: $\langle RM \rangle$ in the cluster rest frame; Col 4: fit error; Col 5: number of sampled beams.

and X-ray large-scale filament, but still within the virial radius of MACS J0717 proper. A crude estimate of the gas density here is $7 \pm 1 \times 10^{-4} \text{ cm}^{-3}$. Deriving the magnetic field from RM using Eq. (3) requires knowledge of the correlation-length scale (Λ_B) of the magnetic field (see Murgia et al. 2004). The expectation value of the RM is in fact:

$$\langle RM^2 \rangle \propto \Lambda_B \int (n_e(l) B_{\parallel}(l))^2 dl \quad (4)$$

We have then to make some assumptions on Λ_B , and to fix the limits of the integral in Eq. (4). If we assume that both gas and magnetic field are uniform on a scale $\Lambda = 1 \text{ Mpc}$ (i.e. the projected distance from B to the center of the main cluster), and that $\Lambda_B = 1 \text{ Mpc}$ as well, we derive $\langle B \rangle \sim 0.5 \mu\text{G}$. This value should be considered a lower limit to the magnetic field strength. In fact, if we assume $\Lambda_B = 200 \text{ kpc}$ (the approximate linear extent of source B), we obtain $\langle B \rangle \sim 1.2 \mu\text{G}$. Although these estimates rely on several assumptions, the values of both the RM and of the magnetic field obtained are still higher than what has been observed previously in sources located at such large distances from the cluster center (see e.g. Clarke et al. 2004). Our findings thus indicate that the magnetic field has already been amplified in these regions, possibly by energetic phenomena associated with the complex merging history of this cluster.

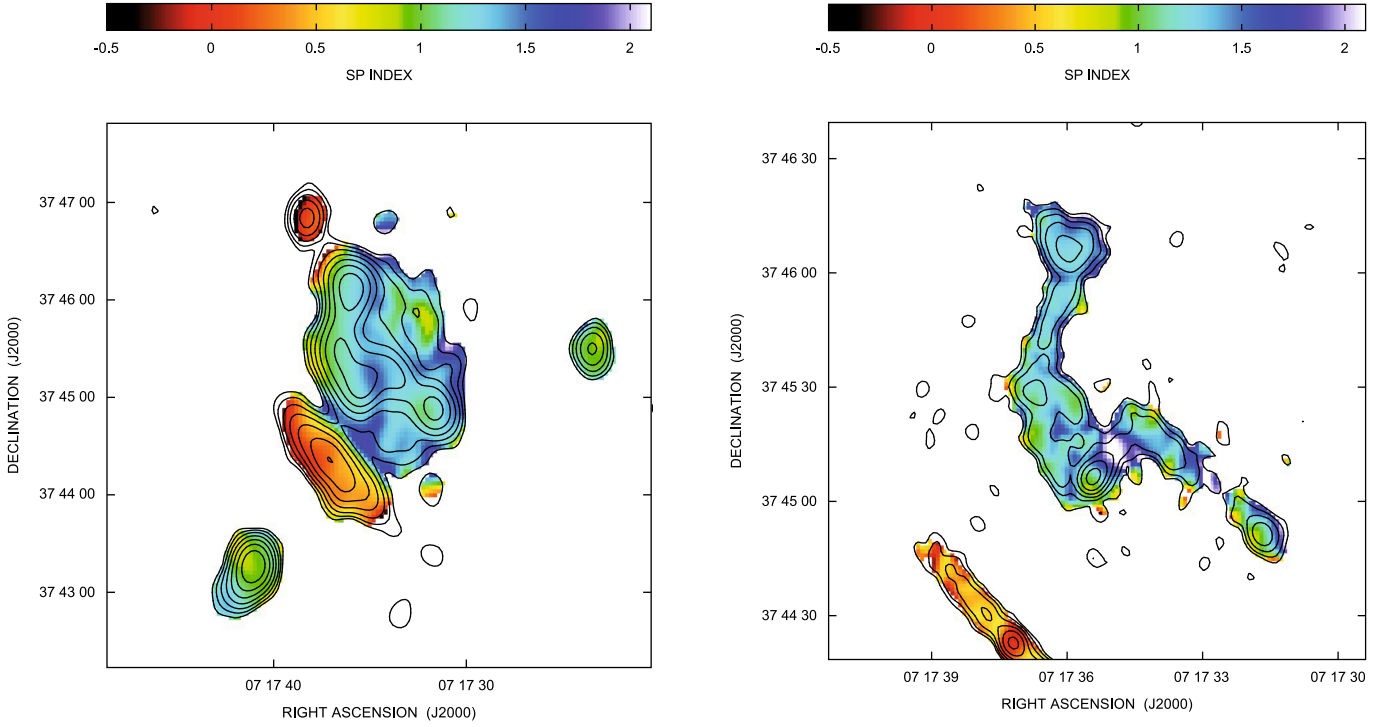


Fig. 7. *Left:* spectral index image of the radio halo between 1.365 GHz and 4.885 GHz. Contours refer to the radio emission at 4.860 GHz. They start at 3σ and are then spaced by a factor of 2. The restoring beam $FWHM$ is $18'' \times 14''$. *Right:* spectral index image of the relic-filament between 1.365 GHz and 4.885 GHz. Contours refer to the radio emission at 4.885 GHz. They start at 3σ and are then spaced by a factor of 2. The restoring beam $FWHM$ is $5'' \times 4''$.

9. Spectral index analysis

The analysis of the spectral index is useful to determine the energetic spectrum of the emitting particles. In fact, it is well known that if the emitting particle energy distribution follows a power law $N(E) \propto E^{-\delta}$ the radio synchrotron spectrum will result to be a power law as well $S(\nu) \propto \nu^{-\alpha}$, with $\alpha = (\delta - 1)/2$.

We derived the spectral index image by comparing the high resolution images at 1.365 and 4.885 GHz and the low resolution images at 1.425 and 4.860 GHz. Spectral index images are shown in Fig. 7. They were obtained considering only pixels whose brightness is $>3\sigma$ at both frequencies. Images at the same resolution were obtained using the same UV-range in order to avoid any effect due to their different sensitivity to the large angular structure.

We computed the global spectral index of the relic-filament by fitting the integrated brightness as a function of the frequency as:

$$\text{Log } S(\nu) = -\alpha \text{Log}(\nu). \quad (5)$$

We obtained $\alpha \sim 1.3 \pm 0.1$ for the relic-filament, from high resolution images, 1.27 ± 0.02 for the radio halo once both the relic-filament and the embedded sources are masked, and 1.27 ± 0.01 for the entire diffuse radio emission (i.e. masking the embedded sources only). The fits are shown in Fig. 8. We have to consider here that the halo emission observed at 4.680 GHz is likely affected by the Sunayev-Zeldovich effect, that causes a decrement of the radio emission at 4.860 GHz and consequently a steepening of the spectral index (see e.g. Liang et al. 2000).

The analysis performed in the previous Secs. indicates that the high resolution emission previously classified as relic is likely a bright region connected with the radio halo itself, rather than a peripheral radio relic. Also the spectral index analysis

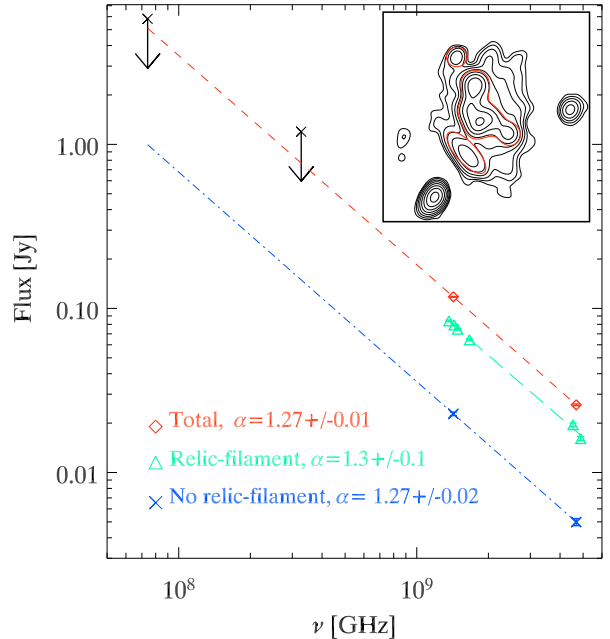


Fig. 8. Global spectral index fit for the relic-filament (triangles), for the halo once the relic-filament is subtracted (crosses) and for the total ICM emission (diamonds) between 20 cm and 6 cm. Arrows represent the upper-limits derived from the VLSS and WENSS. Bars represent 3σ errors. In the inset thick lines illustrate the regions that have been masked in order to obtain the spectral index of the halo once the relic-filament is subtracted.

agrees with this hypothesis since the spectral index of the relic-filament alone, of the halo once the relic-filament is masked and of the entire ICM radio emission has the same value.

Table 4. Radio halo parameters.

Freq GHz	Beam "×"	Flux mJy	LLS Mpc
1.425	21 × 18	118 ± 5	1.5
4.860	18 × 14	26 ± 1	1.0
0.325	84 × 54	1.2 ± 0.5 × 10 ³	1.8
0.740	80 × 80	5.8 ± 0.6 × 10 ³	1.3

Data at 74 and 325 MHz refer to the entire radio emission from the cluster, data at 1.425 and 4.860 GHz refer to the whole extended structure excluding only the contribution of the embedded sources.

The analysis of the spectral index profile in the relic-filament offers another possibility to check this hypothesis. The spectral index study of radio relics has been performed so far on some clusters (see e.g. A2256, Clarke & Ensslin 2006; A3667, Roettgering et al. 1997; A2744, Orrù et al. 2007; A521, Giacintucci et al. 2008; A2345 and A1240, Bonafede et al. 2009), and all of the present theoretical models require the presence of a shock wave that either accelerates the particles from the thermal pool to relativistic energies (Ensslin et al. 1998; Roettiger et al. 1999; Hoeft & Brueggen 2007) or compresses a region containing fossil radio plasma amplifying the magnetic field and re-energizing the particles so that they can emit radio wave again (Ensslin & Gopal-Krishna 2001). In both of these cases a spectral steepening across the relic main axis is expected if the relic is seen edge-on. The particles accelerated or energized by the shock wave lose rapidly their energy because of the combined effect of synchrotron and Inverse-Compton losses. Their particle energy spectrum will thus steepen rapidly giving rise to a radio spectrum that progressively steepens with the distance from the current location of the shock.

In order to investigate the presence of such a systematic trend, we integrated the radio brightness at each frequency (S_ν) in boxes of $\sim 15''$ in width. The associated error is then given by $\sigma_{\text{noise}} \times \sqrt{N_{\text{beams}}}$, with σ_{noise} being the rms noise of the radio image, and N_{beams} the number of beams sampled in each box. The boxes are parallel to the relic main axis, and are shown in the inset of Fig. 9. The spectral index in each box was computed by fitting Eq. (5).

The value of α goes from 1.4 ± 0.2 in the inner box to 1.1 ± 0.1 in the outer box, with values of 1.2 ± 0.1 and 1.3 ± 0.1 in the internal boxes. Its trend does not show a clear progressive steepening as in the case of the other relics cited above. Although we cannot exclude that this is due to ad-hoc projection effects, this result agrees with the hypothesis that the relic-filament is part of the more extended emission that is detected with low resolution observations, i.e. it is a bright filament belonging to the radio halo itself.

Thus, in the following analysis we will consider the flux emitted by the whole extended structure (low resolution emission +relic-filament), excluding only the contribution of the embedded sources. We will refer to this whole emission as halo.

9.1. Spectral index of the radio halo

The total flux of the radio halo at 1.425 GHz and at 4.680 GHz are ~ 118 mJy and ~ 26 mJy respectively. This makes MACS J0717 the most powerful radio halo ever observed. Its radio luminosity at 1.425 GHz, once the k-correction is accounted for, is in fact $\sim 1.6 \times 10^{26}$ WHz⁻¹.

The total flux have been computed over the same area, excluding the regions where the embedded sources are present, so that these values underestimate the total flux of the radio halo

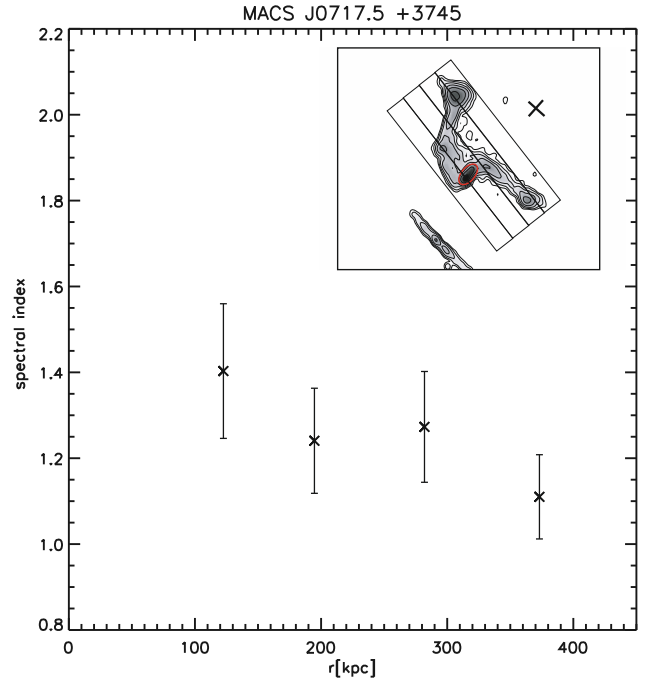


Fig. 9. Spectral index profile between 1.365 and 4.885 GHz as a function of the distance from the cluster center. In the top right inset the displacement of the boxes is shown, the cross marks the location of the center.

and should be regarded as indicative estimates. Due to the low resolution of both the VLSS and the WENSS radio images, it is not possible to resolve the halo and the embedded sources as different radio components, so that the radio flux measured in those images can just be considered as upper limits to the halo spectrum. In Fig. 8 the flux density at the different frequencies are shown. 74 MHz and 325 MHz limits are consistent with the spectral index derived from the 1.425 and 4.680 GHz images.

The distribution of the spectral index is an important observable in a radio halo, since it depends on the shape of the electron spectrum and on the magnetic field in which they emit. Regions of flatter spectra indicate the presence of more energetic particles and/or higher value of the magnetic field strength. A systematic variation of the radio halo spectral index with radial distance from the cluster center is predicted by re-acceleration models (see e.g. Brunetti et al.). In the re-acceleration scenario, in fact, particles are accelerated up to a maximum energy that is given by the balance between acceleration efficiency and energy losses. This results in a break in the spectrum emitted by these electrons. The break frequency depends on the acceleration efficiency and on the magnetic field strength, so that allowing for a decrease of the magnetic field strength with the radius, (see Sect. 10) a radial steepening of the radio spectrum is expected, even in the case of a radial constant acceleration efficiency (see Brunetti et al. 2001; Brunetti 2003; Feretti et al. 2003 and references therein). This radial steepening has been observed in some cases (see e.g. Feretti et al. 2004), while no steepening has been found in Abell 2744 (Orrù et al. 2006). Here it is tricky to derive such a trend since the cluster is in a very complex dynamical state. Ma et al. (2009) suggest that the most massive structure is located at RA $\sim 07^{\text{h}}17^{\text{m}}35^{\text{s}}$, Dec $\sim 37^{\text{d}}45^{\text{m}}00^{\text{s}}$, that is not coincident with the X-ray brightest region. The halo at 1.425 GHz is more extended than at 4.680 GHz. In order to take this properly into account in the spectral index analysis, we integrated the brightness at 1.425 GHz and at 4.860 GHz in radial shells of $\sim 10''$ in

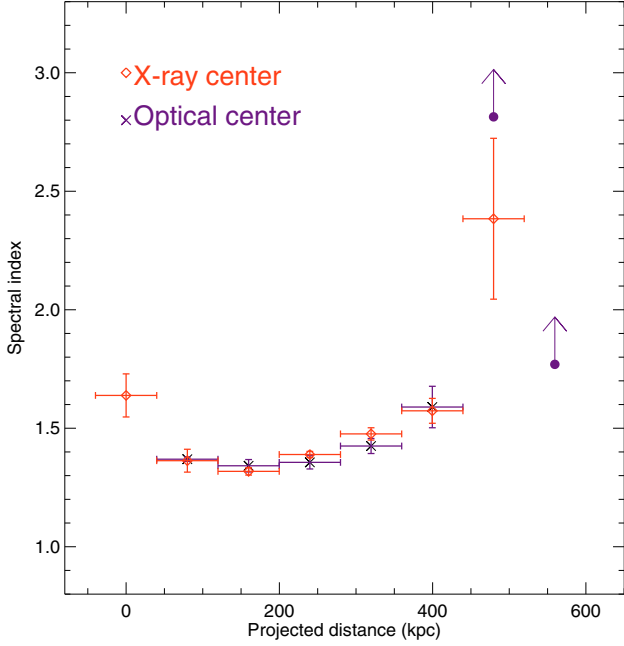


Fig. 10. Spectral index profile of the radio emission observed at low resolution (including the extended emission and the relic-filament region) computed in spherical shells of $10''$ in width. Crosses represent the profile when shells are centered on the X-ray brightness peak, diamonds represent the profile once the shells are centered on the optical integrated light concentration.

width wherever the 1.4 GHz brightness is $>3\sigma$. The associated error is then $\sigma \times \sqrt{N_{\text{beam}}}$. In those shells where the brightness is $>3\sigma$ in the 1.4 GHz image but $<3\sigma$ in the 4.680 GHz image only lower limits on the mean spectral index can be derived. We centered these shells on the X-ray cluster center and on the optical condensation peak. The spectral index profile is shown in Fig. 10. The flattest spectral index value is in the shell that is 150 projected kpc from either the X-ray and the optical center. Higher values of α are found in the shells with radial distances <150 kpc and >200 kpc. A radial steepening is thus detected centered on this point.

9.1.1. Spectral index - X-ray emission

Radio properties of radio halos are linked to the properties of the host cluster. This is directly demonstrated by several correlations that have been found between the radio power and the cluster X-ray luminosity (Bacchi et al. 2003), between the radio power and the thermal gas temperature (Liang et al. 2000), between the radio power and the total cluster mass (Govoni et al. 2001) and between the radio spectral index and the thermal gas temperature (Feretti et al. 2004; Orrù et al. 2006). Recently, Giovannini et al. (in prep) have obtained a correlation between the radio halo integrated spectral index and the average X-ray gas temperature for a large sample of nearby radio halos. According to this correlation cold clusters ($T < 8$ keV) show steep radio spectra (average spectral index = 1.7), while hot clusters ($T > 10$ keV) show an average spectral index = 1.1–1.2. The radio spectrum of present radio halo with $\alpha \sim 1.27$ confirms that flatter spectra are present in high temperature merging clusters.

A spatial comparison of the spectral index image and the X-ray brightness image is shown in the left panel of Fig. 11. There is no clear correlation between the radio halo spectral index and the X-ray emission. We note however that a quite flat

spectral feature is present in the NW region of the radio halo, close to one of the X-ray peaks. With the help of the temperature map (kindly supplied by C.J. Ma), we further investigate the anti-correlation between the spectral index of the radio halo and the ICM temperature. It is expected that flat spectrum regions have higher temperature, since a fraction of the gravitational energy, dissipated during mergers in heating thermal plasma, is converted into re-acceleration of relativistic particles and amplification of the magnetic field. In the right panel of Fig. 11 the temperature map is shown (Ma et al. 2009). A flatter region is detected in the NW part of the radio halo, where the mean temperature is 10.2 ± 2.4 keV (Ma et al. 2009). However, in general, it is difficult to match the patchiness morphology of the temperature map with the spectral index map.

We also investigate the anti-correlation between the ICM temperature and the radio spectral index by computing the spectral index value in regions selected on the basis of their temperature. We used the temperature map obtained after the re-binning process (bottom panel of Fig. 2 in Ma et al. 2009). In Fig. 12 the temperature versus the spectral index is shown. We note that the coldest region is also characterized by the most steep spectrum, but in general from this plot we can gather that a correlation, if present, is weak in this cluster. We argue that it is due to projection effects.

10. ICM magnetic field

The radio analysis performed so far can give important information about the magnetic field in this cluster.

Under the assumption that a radio source is in a minimum energy condition it is possible to derive an average estimate of the magnetic field strength in the emitting volume. We indicate with γ the emitting particle Lorentz factor. The synchrotron luminosity is calculated from a low-energy cut-off of $\gamma_{\text{min}} = 100$ and $\gamma_{\text{max}} \gg \gamma_{\text{min}}$ is assumed. We assume that the emitting particle energy distribution is well represented by a power-law $N(E) \propto E^{-\delta}$ with $\delta = 2\alpha + 1$ in this energy range. The volume of the halo is represented by an ellipsoid having the major and minor axis equal to the maximum and minimum linear extension of the relic, i. e. ~ 1500 kpc and 1200 kpc respectively, and the third axis is assumed to be the mean between the major and the minor one. Under the assumption that magnetic field and relativistic particles fill the whole volume of the source and that the energy content in protons is the same as the one in electrons we find that the equipartition magnetic field is $\sim 1.2 \mu\text{G}$, in agreement with other values found in the literature².

Under equipartition conditions, if we assume that γ_{min} is constant with cluster radius we obtain that

$$j_\nu \propto B^{(\delta+5)/2} \quad (6)$$

where j_ν is the synchrotron emissivity at the frequency ν , B is the magnetic field modulus and δ is the slope of the particle energy distribution.

We used the deprojected brightness profile of the radio halo at 1.425 GHz and computed the equipartition magnetic field radial profile. This is shown in Fig. 13. The deprojected brightness

² Standard equipartition estimate, i. e. obtained computing the radio synchrotron luminosity in a fixed range of frequency (10 MHz–10 GHz) would give $B_{\text{eq}} \sim 0.6 \mu\text{G}$. We report this value to compare this estimate with other given in the literature for other radio-sources. However it has been pointed out by Brunetti et al. (1997) that this approach is not self-consistent since electron energy corresponding to a fixed frequency depends on the magnetic field value.

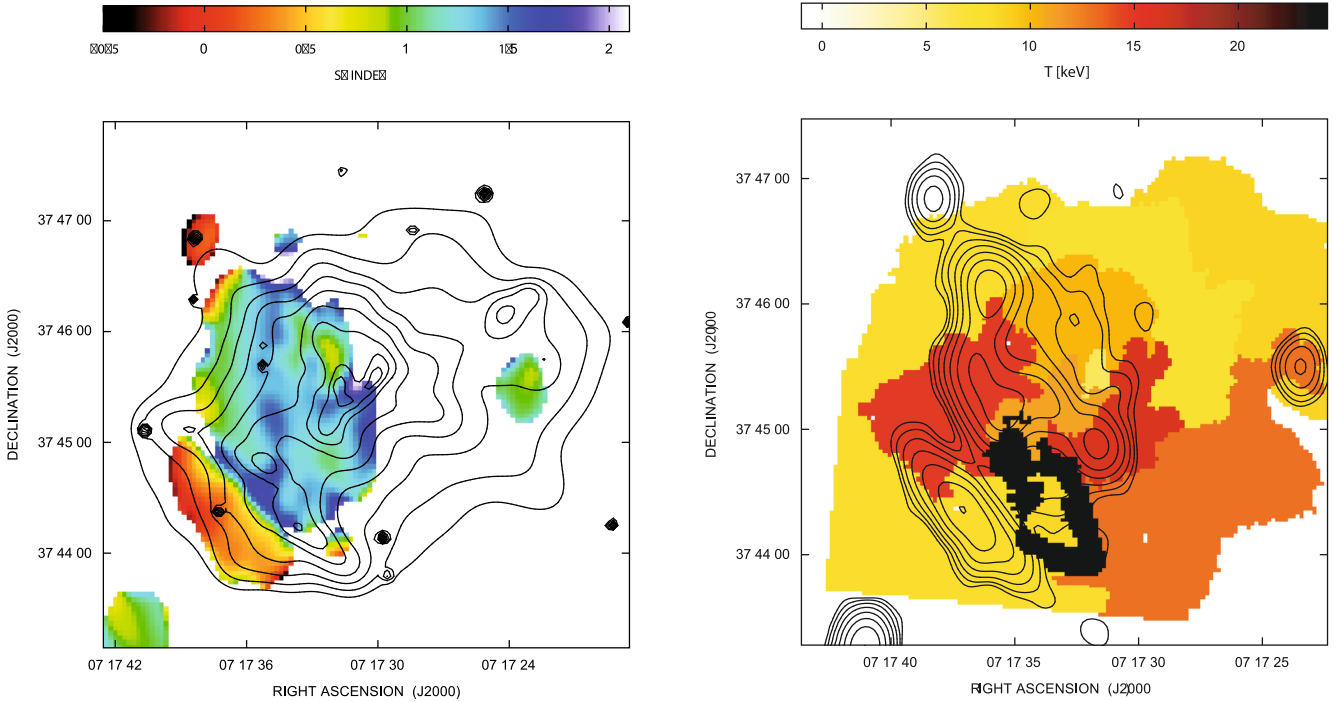


Fig. 11. *Left:* Spectral index map overlaid onto X-ray contours. Contours refer to the Chandra X-ray emission in the 0.7-5 keV band. Contours start at 0.06 counts/s and are spaced by $\sqrt{2}$. *Right:* temperature map (from Ma et al. 2009) overlaid onto radio contours at 4.860 GHz. They start at 3σ and are then spaced by a factor of 2. The restoring beam $FWHM$ is $18'' \times 14''$.

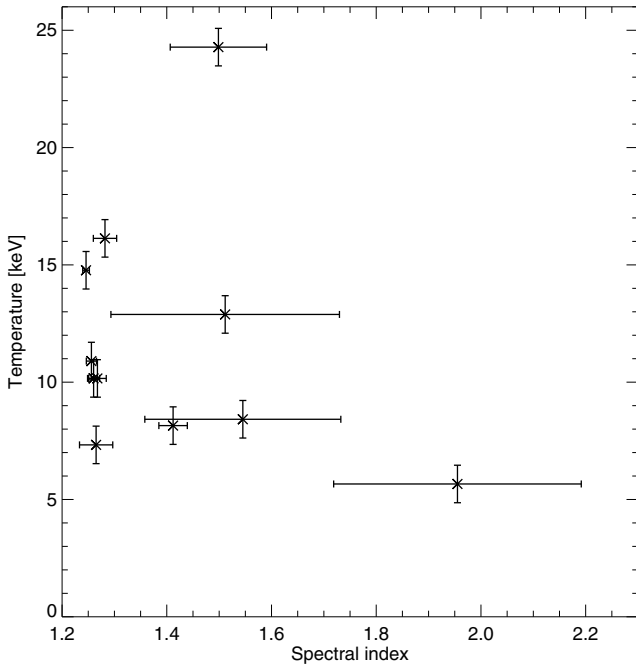


Fig. 12. Temperature versus spectral index.

profile was computed assuming spherical symmetry with respect to the radio peak brightness. The equipartition magnetic field decreases by a factor ~ 2.5 from the center to the periphery of the cluster. If the cluster magnetic field decreases with radius as:

$$B(r) = B_0 \left[1 + \frac{r^2}{r_c^2} \right]^{-\frac{3\mu}{2}} \quad (7)$$

it is possible to reproduce the equipartition magnetic field profile assuming $\mu = 1.1$, i.e. assuming that the magnetic field profile scales as the gas density profile. Once μ is fixed, it is possible to derive the value of B_0 necessary to reproduce the magnetic field equipartition estimate. We obtain that $B_0 = 3 \mu\text{G}$ averaged over the halo emitting volume ($\sim 1.1 \text{ Mpc}^3$) can reproduce the equipartition magnetic field estimate.

The detection of polarized emission reveals important information about the magnetic field structure in this cluster. Radio halos are intrinsically polarized, since the synchrotron process generates linearly polarized emission. However, in the ICM the emitting plasma is mixed with the thermal one, so due to the Faraday Rotation significant depolarization may occur. Moreover, radio halos have a low surface brightness, and high resolution observations are often unable to detect them; if the magnetic field is tangled on scales smaller than the beam size, the observed emission will be further depolarized (beam depolarization). These two effects can explain why polarized emission from radio halos is usually non-detected.

The presence of polarized emission here indicates that the magnetic field fluctuates on scales as large as the beam, that is 130 kpc. Murgia et al. (2004) have demonstrated that if the magnetic field power spectrum³ is steep enough ($n > 3$) and the outer scale of the magnetic field fluctuation is larger than few hundreds kpc, it is possible to detect polarized emission from radio halos.

Radio halos are expected to be generated by re-acceleration of particles by Fermi II processes that occur in the ICM after merger events (see e.g. Cassano & Brunetti 2005; Cassano et al. 2006). The energy is injected at large spatial scales and then a turbulent cascade is generated. This cascade converts the energy into motions at smaller and smaller scales until the dissipation

³ The magnetic field power spectrum is modelled as $|B(\Lambda)|^2 \propto \Lambda^n$, where Λ is the fluctuation scale in the real space and n is the power spectrum spectral index

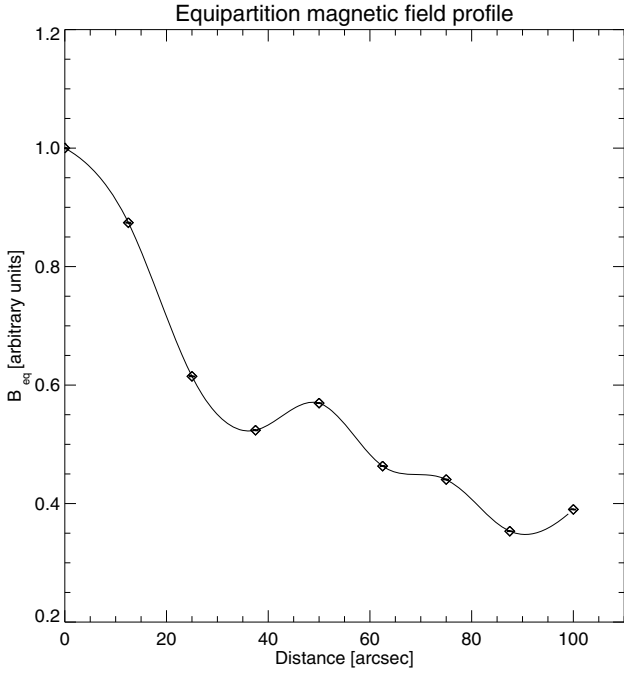


Fig. 13. Equipartition magnetic field radial profile. It has been normalized to its central value. Regions where radio galaxies are present have been masked.

scale is reached. The analysis performed on this cluster suggests that it could be in a young phase after the merger. The magnetic field is thus still ordered on sufficient large scale and its polarized emission can be detected even with low resolution observations.

11. Conclusions

The main result of this work is the discovery of a giant radio halo in a massive galaxy cluster at $z \sim 0.55$. The radio halo of MACS J0717 is the most distant radio halo ever observed and the most powerful one. Moreover, it is only the second halo for which polarized emission has been detected. We here summarize the results of our analysis:

- the cluster MACS J0717+3745 shows a complex radio morphology that reflects the complex dynamical state revealed by X-rays and optical studies;
- a powerful radio halo has been observed, emission from which is detected here for the first time at 1.425 and 4.680 GHz. With a radio power of $\sim 1.6 \times 10^{26} \text{ WHz}^{-1}$ at 1.4 GHz, it is the most powerful radio halo ever observed. Its spectral index is steep ($\alpha = 1.27 \pm 0.01$), in agreement with results obtained for other radio halos found at lower redshifts. Our detection of diffuse radio emission from MACS J0717 at $z = 0.55$ indicates that the ICM is already magnetized at this redshift;
- we argue that the bright radio emission visible in high-resolution images and previously classified as relic is more likely a bright, polarized filament connected with the radio halo. This feature, in fact, lies at the center of the cluster and of the radio halo. The trend of the polarization angle Ψ versus λ^2 indicates that the Faraday rotation originates in a region where a morphologically complex mix of thermal and non-thermal gas is present, resulting in a poor match both with the λ^2 law expected in the case of a Faraday screen and with the simplified model expected in the case of a uniform slab.

Although the effects of depolarization cannot be taken into account trivially, we find the most plausible scenario to be one in which this filamentary emission is embedded in the central cluster region. The radio emission from this filamentary structure is polarized at $\sim 8\%$ at 1.365 GHz and $\sim 17\%$ at 4.885 GHz, and the polarization image does not show any discontinuity between the radio halo and this relic-filament structure. The spectral-index profile further reinforces our interpretation since no clear steepening is observed across the main axis, as would be expected if the emission were caused by a peripheral shock wave. We also note that the mean spectral index of the relic-filament and of the radio halo are fully compatible within the small errors;

- low-resolution polarization observations at 1.425 GHz have shown that the polarized emission is not confined to the bright relic-filament observed at high resolution but extends to the innermost regions of the radio halo and to some regions in the outskirts. Following Murgia et al. (2004), this indicates that the power spectrum of the magnetic field is steep in this cluster, with a spectral index $n > 3$, and that it must fluctuate on scales as large as $\sim 130 \text{ kpc}$;
- under the equipartition assumption, we derived the magnetic-field profile of the radio halo and found it consistent with predictions based on the assumption that the magnetic-field profile scales as the gas-density profile. Once the radial decline is fixed, a central value of $\sim 3 \mu\text{G}$ can also account for the magnetic-field equipartition estimate.

Acknowledgements. We thank C.J. Ma for providing the ICM temperature map for MACS J0717, and A. Mantz for helpful comments. We thank the anonymous referee for useful comments. G.G. is a postdoctoral researcher of the FWO-Vlaanderen (Belgium). H.E. gratefully acknowledges financial support from SAO and STScI under grants GO3-4168X and GO-09722/GO-10420, respectively. NRAO is a facility of the National Science Foundation, operated under cooperative agreement by Associated Universities, Inc. This work was partly supported by the Italian Space Agency (ASI), contract I/088/06/0, by the Italian Ministry for University and Research (MIUR) and by the Italian National Institute for Astrophysics (INAF). This research has made use of the NASA/IPAC Extragalactic Data Base (NED) which is operated by the JPL, California Institute of Technology, under contract with the National Aeronautics and Space Administration. We acknowledge the WENSS team (<http://www.astron.nl/wow/testcode.php>)

References

- Bacchi, M., Feretti, L., Giovannini, G., & Govoni, F. 2003, *A&A*, 400, 465
 Bonafede, A., Giovannini, G., Feretti, L., Govoni, F., & Murgia, M. 2009, *A&A*, 494, 429
 Brunetti, G. 2003, *ASPC*, 301, 349
 Brunetti, G., Setti, G., & Comastri, A. 1997, *A&A*, 325, 898
 Brunetti, G., Setti, G., Feretti, L., & Giovannini, G. 2001, *MNRAS*, 320, 365
 Brunetti, G., Giacintucci, S., Cassano, R., et al. 2008, *Natur*, 455, 944
 Burn, B. J. 1966, *MNRAS*, 133, 67
 Carilli, C. L., & Taylor, G. B. 2002, *ARA&A*, 40, 319
 Cassano, R., & Brunetti, G. 2005, *MNRAS*, 357, 1313
 Cassano, R., Brunetti, G., & Setti, G. 2006, *MNRAS*, 369, 1577
 Cavaliere, A., & Fusco-Femiano, R. 1976, *A&A*, 49, 137
 Clarke, T. E. 2004, *JKAS*, 37, 337
 Clarke, T. E., & Ensslin, T. A. 2006, *AJ*, 131, 2900
 Cohen, A. S., Lane, W. M., Cotton, W. D., et al. 2007, *AJ*, 134, 1245
 Dolag, K., & Staszyszyn F. A. 2008, [[arXiv:0807.3553](https://arxiv.org/abs/0807.3553)]
 Dolag, K., Vogt, C., & Enßlin, T. A. 2005, *MNRAS*, 358, 726
 Dolag, K., Bykov, A. M., & Diaferio, A. 2008, *SSRv*, 134, 311
 Donnert, J., Dolag, K., Lesch, H., & Müller, E. 2009, *MNRAS*, 392, 1008
 Ebeling, H., Edge, A. C., & Henry, J. P. 2001, *ApJ*, 553, 668
 Ebeling, H., Barrett, E., & Donovan, D. 2004, *ApJ*, 609, L49
 Ebeling, H., White, D. A., & Rangarajan, F. V. N. 2006, *MNRAS*, 368, 65
 Ebeling, H., Barrett, E., Donovan, D., et al. 2007, *ApJ*, 661, L33
 Edge, A. C., Ebeling, H., Bremer, M., et al. 2003, *MNRAS*, 339, 913

- Ensslin, T. A., Biermann, P. L., Klein, U., & Kohle, S. 1998, *A&A*, 332, 395
- Enßlin, T. A., & Gopal-Krishna 2001, *A&A*, 366, 26
- Feretti, L. 2003, *ASPC*, 301, 143
- Feretti, L., Dallacasa, D., Giovannini, G., & Tagliani, A. 1995, *A&A*, 302, 680
- Feretti, L., Orrù, E., Brunetti, G., et al. 2004, *A&A*, 423, 111
- Ferrari, C., Govoni, F., Schindler, S., Bykov, A. M., & Rephaeli Y. 2008, *SSRv*, 134, 93
- Giacintucci, S., Venturi, T., Macario, G., et al. 2008, *A&A*, 486, 347
- Giovannini, G., & Feretti, L. 2000, *NewA*, 5, 335
- Govoni, F., & Feretti, L. 2004, *IJMPD*, 13, 1549
- Govoni, F., Feretti, L., Giovannini, G., et al. 2001, *A&A*, 376, 803
- Govoni, F., Murgia, M., Feretti, L., et al. 2005, *A&A*, 430, L5
- Govoni, F., Murgia, M., Feretti, L., et al. 2006, *A&A*, 460, 425
- Hoft, M., & Brügger, M. 2007, *MNRAS*, 375, 77
- Johnston-Hollitt, M., & Ekers, R. D. 2004, [arXiv:astro-ph/0411045]
- Kim, K.-T., Kronberg, P. P., & Tribble, P. C. 1991, *ApJ*, 379, 80
- Liang, H., Hunstead, R. W., Birkinshaw, M., & Andreani, P. 2000, *ApJ*, 544, 686
- Ma C.-J., Ebeling H., Donovan, D., & Barrett, E. 2008, *ApJ*, 684, 160
- Ma, C.-J., Ebeling, H., & Barrett, E. 2009, *ApJ*, 693, L56
- Murgia, M., Govoni, F., Feretti, L., Giovannini, G., Dallacasa, D., et al. 2004, *A&A*, 424, 429
- Orrù, E., Murgia, M., Feretti, L., et al. 2007, *A&A*, 467, 943
- Rengelink, R. B., Tang, Y., de Bruyn, A. G., et al. 1997, *A&AS*, 124, 259
- Rottgering, H. J. A., Wieringa, M. H., Hunstead, R. W., & Ekers, R. D. 1997, *MNRAS*, 290, 577
- Roettiger, K., Burns, J. O., & Stone, J. M. 1999, *ApJ*, 518, 603
- Simard-Normandin, M., Kronberg, P. P., & Buton, S. 1981, *ApJS*, 45, 97
- Taylor, G. B., & Perley, R. A. 1993, *ApJ*, 416, 554